

1 **General Response: We thank the Referee for your helpful comments. We have addressed**
2 **the comments and provided response below. The revised manuscript is presented in below**
3 **Response**

4

5 Thank you for the careful consideration of the reviewers' comments. The manuscript has been
6 largely improved. The low-magnification TEM image (Fig. 7) helps understand the samples.
7 Although the figure is useful, I recommend showing more soot particles in all TEM images,
8 i.e., Fig. 7 (a) has no fresh soot image, and Fig 7(b) only has one soot particles. Overall, the
9 revised manuscript looks well.

10 **Answer: We appreciated the Referee#1's comments which significantly improve the quality of**
11 **the manuscript. We provided more TEM images of dominated soot type at T1, T2, and T3. The**
12 **newly added soot images were presented as Figure 7a2-c2.**

13

14 **Tracing the evolution of morphology and mixing state of soot**

15 **particles along with the movement of an Asian dust storm**

16 Liang Xu¹, Satoshi Fukushima², Sophie Sobanska³, Kotaro Murata², Ayumi Naganuma², Lei Liu¹,

17 Yuanyuan Wang¹, Hongya Niu⁴, Zongbo Shi⁵, Tomoko Kojima⁶, Daizhou Zhang², Weijun Li^{1,*}

18 ¹Department of Atmospheric Sciences, School of Earth Sciences, Zhejiang University, Hangzhou

19 310027, China

20 ²Faculty of Environmental and Symbiotic Sciences, Prefectural University of Kumamoto,

21 Kumamoto 862-8502, Japan

22 ³Institute of Molecular Sciences, UMR CNRS 5255, University of Bordeaux, 351 cours de la

23 libération, 33405 Talence, France

24 ⁴Key Laboratory of Resource Exploration Research of Hebei Province, Hebei University of

25 Engineering, Handan 056038, Hebei, China

26 ⁵School of Geography, Earth and Environmental Sciences, University of Birmingham, UK

27 ⁶Department Earth and Environmental Science, Faculty of Advanced Science and Technology,

28 Kumamoto University, Kumamoto 860-8555, Japan

29

30 *Corresponding author: W. Li (liweijun@zju.edu.cn)

31 Department of Atmospheric Sciences, School of Earth Sciences, Zhejiang University, Hangzhou

32 310027, China

33

34

35

36 **Abstract**

37 Tracing the aging progress of soot particles during transport is highly challenging. An
38 Asian dust event could provide an ideal opportunity to trace the continuous aging
39 progress of long-range transported soot particles. Here, we collected individual aerosol
40 particles at an inland urban site (T1) and a coastal urban site (T2) in China and a coastal
41 site (T3) in southwestern Japan during an Asian dust event. Microscopic analysis
42 showed that the number fraction of soot-bearing particles was 19% and 16% at T1 and
43 T2 in China but surprisingly increased to 56% at T3 in Japan. The dominant fresh soot
44 (71%) at T1 became partially embedded (68%) at T2 and fully embedded (84%) at T3.
45 These results indicated that the tiny soot particles had lower deposition than other
46 aerosol types and became more aged during the transport from T1 to T3. We quantified
47 soot morphology using the fractal dimension and found the trend from 1.65 at T1, 1.84
48 at T2, and to 1.91 at T3. Furthermore, we found that the morphology compression of
49 the soot aggregations was associated with secondary coating thickness and relative
50 humidity. A unique mixing structure that multi-soot particles scattered in organic
51 coatings instead of sulfate core in individual core-shell particles was observed at T3
52 after the crossing of the East China Sea. The study well understands important
53 constraints of the soot morphological effects and provides possible aging scale along
54 with their transport pathway. These new findings will be helpful to improve optical
55 calculation and regional climate modeling of soot particles during their transport in the
56 atmosphere.

57

58 **1. Introduction**

59 Soot (i.e., black carbon (BC)) is a type of carbonaceous material with graphitic
60 structures emitted from the incomplete combustion of fossil fuels and biomass. Soot
61 particles exhibit a chain-like aggregation morphology with a diameter of 10 nm to 100
62 nm (Buseck et al., 2014). Because of its strong capacity to absorb solar radiation, soot
63 is considered the second greatest contributor to global warming after carbon dioxide
64 (IPCC., 2013;Bond et al., 2013). Soot is an important particulate pollutant in fine
65 particles (i.e., PM_{2.5}) in urban polluted air, which adversely affects the respiratory health
66 of citizens and induces generally unwanted heating in the planetary boundary layer
67 (West et al., 2016;Ding et al., 2016).

68 Fresh soot particles are hydrophobic but are converted into a hydrophilic state
69 following their aging through physical and chemical processes (Li et al., 2016b;Riemer
70 et al., 2010;Perring et al., 2017). Aged soot particles containing secondary coating
71 aerosols (e.g., ammonium sulfate, ammonium nitrate, and organic matter) can be
72 activated as cloud condensation nuclei (CCN) (Zhang et al., 2008;Wang et al.,
73 2010;Ding et al., 2019;Shiraiwa et al., 2007;Lee et al., 2019). These coatings can
74 significantly change the optical scattering and absorption capacity of soot particles (Liu
75 et al., 2017;Moffet and Prather, 2009;Matsui et al., 2018;He et al., 2015;Zhang et al.,
76 2018a). Numerical model simulations have estimated that light absorption by internally
77 mixed soot is enhanced by a factor of 2 over externally mixed soot (Jacobson, 2001).
78 In contrast, Cappa et al. (2012) reported in situ observations of soot absorption
79 enhancement of only 6% in ambient air. This discrepancy between simulation and

80 observation could be attributed to the complex mixing structure and various
81 morphologies of soot particles in the air (Adachi et al., 2016;Li et al., 2016a;Wu et al.,
82 2018).

83 In aged air masses, soot particles tend to be internally mixed with secondary
84 aerosols such as sulfates, nitrates, and secondary organic matter (Li et al., 2016b).
85 Especially in the East Asian region, one of the most polluted areas in the world, soot is
86 internally mixed with secondary aerosols in polluted urban, rural, and remote air
87 (Adachi et al., 2016;Zhang et al., 2013;Yuan et al., 2019;Zhang et al., 2018b). However,
88 most of these studies have focused on the aging and mixing state of soot particles at one
89 or multiple isolated sites. These results have not traced the detailed aging processes
90 (e.g., morphology and mixing structure) from fresh to aged soot particles during their
91 transport.

92 Although great progress has been made in the field of soot aging, it is highly
93 challenging to trace the aging processes of soot particles during transport. Asian dust
94 storms carry both dust and anthropogenic aerosols across East Asia into the North
95 Pacific Ocean (Li et al., 2014;Geng et al., 2014;Zhang et al., 2005). This presents an
96 ideal environment to study the aging processes of soot particles during long-range
97 transport. Compared to previous publications, the present study quantified the variation
98 in mixing structures and fractal dimension of soot particles and further explored how
99 shape of soot particles changed following the dust storm movement from East China to
100 Japan.

101 Using transmission electron microscopy (TEM), we investigated the morphology,

102 mixing structure, relative abundance, and size distribution of individual soot particles.
103 Furthermore, we evaluated the morphological differences of individual soot particles at
104 three sampling sites. Finally, a conceptual model was proposed to better understand the
105 aging processes of long-rang transported soot particles.

106 **2. Experimental methods**

107 **2.1 Aerosol sampling**

108 Three sampling sites were chosen for aerosol collections: an inland urban site in
109 Jinan city (T1, 36.67°N 117.06°E), China, a coastal urban site in Qingdao city (T2,
110 36.10°N 120.46°E), China, and a coastal rural site at Amakusa (T3, 32.30°N 130.00°E)
111 in southwestern Japan (Figure 1). A dust storm outbreak was observed in East Asia.
112 Detailed information about this dust storm will be discussed in Section 3.1. We
113 collected aerosol particles during dust transport from 18 to 19 March 2014 at the three
114 sampling sites (Figure S1-S5). In total, seven dust samples were collected within 30
115 hours after the dust storm arrival. The details about the sampling dates, times,
116 meteorological conditions, and PM (particulate matter) concentrations for the samples
117 are listed in Table S1.

118 A DKL-2 sampler (Genstar Electronic Technology, China) was used to collect
119 individual aerosol particles on copper TEM grids covered by carbon film (carbon type-
120 B, 300-mesh copper; Tianld Co., China) with an air flow of 1.0 L/min. A single-stage
121 impactor with a 0.5 mm diameter jet nozzle was installed on the sampler. This impactor
122 has a collection efficiency of 100% at an aerodynamic diameter of 0.5 μm with an
123 assumed particle density of 2 g/cm^3 . The sampling duration varied from 1 min to 2 min

124 according to the visibility, PM concentration, and particle distribution on the substrate.
125 All samples were placed in sealed, dry plastic capsules and stored in a desiccator at
126 25 °C and $20 \pm 3\%$ relative humidity (RH) for further analysis.

127 **2.2 Electron microscopic analyses**

128 A JEOL JEM-2100 transmission electron microscopy (TEM) operated at 200 kV
129 was used to analyze individual particles. Elemental composition was determined
130 semiquantitatively by using an energy-dispersive X-ray spectrometer (EDS) (Oxford
131 Instruments, UK) that can detect elements heavier than carbon ($Z \geq 6$). The distribution
132 of aerosol particles on TEM grids was not uniform, with coarser particles occurring
133 near the center and finer particles occurring on the periphery (Xu et al., 2019). Therefore,
134 to ensure that the analyzed particles were representative of the entire size range, three
135 areas were chosen from the center to the periphery of the sampling spot on each grid.
136 iTEM software (Olympus Soft Imaging Solutions GmbH, Germany) was used to
137 analyze the TEM images and obtain the projected area, perimeter, shape factor, and
138 equivalent circle diameter (ECD) of individual aerosol particles. In total, we analyzed
139 412, 486, and 887 aerosol particles for T1, T2, and T3 site, respectively.

140 **2.3 AFM analysis**

141 Atomic force microscopy (AFM) is an analytical method used for studying the
142 surface structure of solid materials. AFM (Dimension Icon, Germany) can determine
143 the three-dimensional morphology of particles in tapping mode. The AFM settings
144 consisted of imaging forces between 1 and 1.5 nN, scanning rates between 0.5 and 0.8
145 Hz, and a scanning range of 10 μm with a resolution of 512 pixels per length. The

146 bearing areas (A) and bearing volumes (V) of the particles were directly obtained from
147 NanoScope Analysis software. Their equivalent circle diameters (ECDs) and equivalent
148 volume diameters (EVDs) were calculated according to the formulas described by Chi
149 et al. (2015).

150 The correlations of ECDs and EVDs are shown in Figure S6 in the Supporting
151 Information. Therefore, the ECD of individual aerosol particles measured from the
152 iTEM software can be further converted into an EVD based on this correlation.

153 **2.4 Air mass backward trajectories**

154 Forty-eight hour backward trajectories were calculated for the three sites using the
155 NOAA HYSPLIT (Hybrid Single Particle Lagrangian Integrated Trajectory) trajectory
156 model (Stein et al., 2015). We selected an altitude of 1500 m as the end point in each
157 backward trajectory.

158 We measured the actual duration from the Beijing-Tianjin-Hebei (BTH) area to T1
159 and T2 according to the backward trajectories in Figure 1. It was approximately 12
160 hours between BTH and T1 and 15 hours between BTH and T2. The interval between
161 T1 and T2 was three hours. The duration between the air mass leaving T2 and reaching
162 T3 was approximately 30 hours.

163 **2.5 Morphological analysis of soot particles**

164 The fractal dimension (D_f) calculated by the scaling law is used to characterize the
165 morphology of soot particles (Koeylue et al., 1995).

$$166 \quad N = k_g \left(\frac{2R_g}{d_p} \right)^{D_f} \quad (1)$$

167 where N is the total number of soot monomers, R_g is the radius of gyration of the soot

168 particle, d_p is the diameter of soot monomer, k_g is the fractal prefactor, and D_f is the
169 mass fractal dimension of an individual soot particle.

170 D_f and k_g in Equation 1 are estimated from a power law fit of a scatter plot of N
171 versus the values of $2R_g/d_p$. N can also be calculated by Equation 2.

$$172 \quad N = k_a \left(\frac{A_a}{A_p} \right)^\alpha \quad (2)$$

173 where A_a is the projected area of the soot particle, A_p is the mean projected area of the
174 soot monomer, k_a is a constant, and α is an empirical projected area exponent.

175 The values of α and k_a in Equation 2 depend on the overlap parameter (δ) calculated
176 using Equation 3. Then δ can be used to obtain α and k_a based on Fig. 6. in Oh and
177 Sorensen (1997).

$$178 \quad \delta = \frac{2a}{l} \quad (3)$$

179 where a is the soot monomer radius and l is the monomer spacing.

180 The radius of gyration of the soot particle R_g is obtained by the simple
181 correlation in Equation 4 developed by Brasil et al. (1999)

$$182 \quad L_{\max}/(2R_g) = 1.50 \pm 0.05 \quad (4)$$

183 where L_{\max} is the maximum length of the soot particle.

184 The values of d_p , A_a , A_p , a , l , and L_{\max} can be directly obtained from TEM images.

185 In addition to D_f , we also used the shape factor (SF) to further quantify the
186 morphological differences of soot particles. The shape factor is defined as the ratio of
187 the actual area of a particle to the area of a circle with the same perimeter (Equation 5).

188 A shape factor of 1 (the maximum value) indicates a perfectly round particle.

$$189 \quad SF = \frac{4\pi S}{P^2} \quad (5)$$

190 where S is the area of a soot particle and P is the perimeter of a soot particle.

191 **3. Results and discussion**

192 **3.1 The Asian dust storm event**

193 Figure 2 displays variations in PM₁₀ and PM_{2.5} concentrations before, during, and
194 after the dust storm event at the Jinan, Qingdao, and Amakusa sampling sites. The dust
195 storm air mass started to influence T1 at approximately 06:00 on 03/17 (Universal Time
196 Coordinated, UTC). The concentration of PM₁₀ at T1 increased rapidly to a maximum
197 value of 834 µg/m³. The air mass reached T2 at 09:00 on 03/17, and the highest PM₁₀
198 concentration was recorded at 721 µg/m³. After the arrival of a cold front at T2, the air
199 mass continued moving approximately 1000 km to T3 at 02:00 on 03/18. The
200 concentration of PM₁₀ reached 87 µg/m³ at T3 (Figure 2). During this study, the
201 meteorological data (e.g., temperature and air pressure) measured at the three sampling
202 sites also confirm the arrival time of the dust storm (Figures S3-S5). All seven dust
203 samples were collected after the arrival of the dust storm, thus confirming the sampling
204 of the same dust storm event (Figures 2 and S2).

205 Figure 1 indicates that all the air masses during the dust storm event originated
206 from Mongolia, moving southeastward via the BTH area, reaching T1 and T2. The BTH,
207 as the largest city cluster in China, contains one of the largest anthropogenic emission
208 sources (e.g., heavy industries, coal-fired power plants, and vehicles) in the world (Li
209 et al., 2016b). The transport duration from the BTH to T1 and T2 was about 12 hours
210 and 15 hours, respectively. Thus, we estimated that the interval between T1 and T2 was
211 three hours. After passing over T1 and T2, the air masses kept moving southeastward
212 to Japan. The estimated interval between T2 and T3 was 30 hours. The ground PM and
213 meteorological measurements at the three sampling sites (Figure 2 and S3-S5) coupled

214 with air mass back trajectories (Figure 1) and a dust storm simulation in East Asia
215 (Figure S1) together verified that the dust storm event, under the force of a strong cold
216 front, transported across the large BTH city cluster to the downwind area. Therefore,
217 this dust storm movement provides a unique opportunity to study particles in the same
218 air mass and thus trace physical and chemical changes in aerosol particles.

219 **3.2 Classification and mixing state of soot-bearing particles**

220 Soot particles with a typical chain-like structure can be easily distinguished from
221 other aerosol components (e.g., sulfate, organic, metal, and mineral particles) by their
222 morphology. TEM observation is a convenient way to determine whether soot is
223 associated with other aerosol components (Li et al., 2016b; Laskin et al., 2019). During
224 the dust storm period, 56% of the analyzed particles within a size range of 50 nm to 2.4
225 μm included soot particles at T3, approximately three times higher than those at T1
226 (19%) and T2 (16%). This high percentage of internally mixed soot particles was also
227 shown by Ueda et al. (2016) in an Asian outflow at Noto Peninsula, Japan, based on
228 single-particle soot photometer (SP2) analyses. Our results show that the dust storm
229 event not only carried large amounts of dust particles from the Gobi Desert in
230 northwestern China but that this dust-laden air mass also incorporated many soot
231 particles from polluted East Asia (Figure 2 and Figure 3a-d). This is consistent with Pan
232 et al. (2015), who showed that dust storms in East Asia contain and transport
233 anthropogenic pollutants from urban areas.

234 Based on the mixing structures between soot and sulfate on the substrates, three
235 groups of soot particles were defined in this study: fresh, partially embedded and fully
236 embedded (Figure 3).

237 *Fresh soot.* The soot particles were not obviously mixed with secondary aerosol

238 components (Figure 3a). Although surfaces of the fresh soot particles could contain
239 minor organic matter, the organic film was insufficient to change soot morphology and
240 optical properties (Buseck et al., 2014).

241 *Partially embedded soot.* Part of the soot particle was coated by secondary aerosols
242 (Figure 3b). Most of partially embedded soot particles include one soot core, only ~ 10%
243 of them contain two soot cores (Figure S7).

244 *Fully embedded soot.* The entire soot particle was encapsulated by secondary
245 aerosols (Figure 3c). It should be noted that some soot particles were only embedded in
246 the organic coating instead of the sulfur-rich core (Figure 3d).

247 TEM images show that the fully embedded soot particles with a clear rim on the
248 substrate displayed a droplet-like shape (Figure 3c-d), suggesting that these secondary
249 particles were in an aqueous phase in ambient air (Li et al., 2016b).

250 Based on the three mixing structures of soot particles, we further obtained their
251 relative abundance at the three sampling sites (Figure 4). Seventy-one percent of soot-
252 bearing particles were fresh at T1, decreasing to 10% at T2. In contrast, partially
253 embedded soot increased from 14% at T1 to 68% at T2 when the cold front moved from
254 T1 to T2. It should be noted that fresh soot disappeared at T3 after crossing the East
255 China Sea, and the fully embedded soot dominated soot-bearing particles (84%).

256 Following the dust storm movement, we found that the number fraction of total
257 soot-bearing particles increased to 56% among all the analyzed particles from T1 to T3,
258 suggesting that soot particles had lower deposition than other aerosol types in the cold
259 front. Indeed, soot particles normally have smaller sizes and densities than mineral dust,

260 metal, sulfate, and nitrate particles (Peng et al., 2017), suggesting that soot particles can
261 be transported over longer distances during Asian dust storms. Moreover, the number
262 fraction increase of soot-bearing particles also could be attributed to the increase of
263 mixing state index (the metric to quantify the population mixing state, ranging from 0
264 for a completely external mixture to 1 for a completely internal mixture) as aging during
265 transport (Riemer and West, 2013; Healy et al., 2014).

266 **3.3 Quantifying the morphology of soot particles**

267 The fractal dimension (D_f) of soot particles is a key parameter used to reflect soot
268 morphological structure; e.g., compact soot particles usually have larger D_f than lacy
269 aggregates (China et al., 2015; Wang et al., 2017; China et al., 2013). Therefore, D_f can
270 be used to understand soot aging processes in the atmosphere. Figure 5 shows that the
271 D_f sequence of soot particles is T1 (1.65) < T2 (1.84) < T3 (1.91). The D_f of soot
272 particles at T1 (1.65) is much closer to the values of soot emitted from sources, such as
273 the D_f from biomass burning in the range of 1.68–1.74 (Chakrabarty et al., 2006) and
274 the D_f from diesel burning in the range of 1.56–1.68 (Wentzel et al., 2003). The D_f of
275 soot particles at T3 (1.96 for partially embedded soot and 1.88 for fully embedded soot,
276 Figure S8) is close to that of aged soot (1.81–1.90) in remote marine air (China et al.,
277 2015) and polluted air in North China (Wang et al., 2017).

278 At the three sampling sites, the highest D_f value at T3 suggests a more compacted
279 structure of the soot particles. Moreover, we obtained the shape factors of soot particles
280 at the three sampling sites to indicate the compactness of soot particle. The average
281 shape factor of soot particles at T3 was 0.73, much higher than 0.34 at T1 and 0.54 at

282 T2 (Figure 6a). These two parameters show that the soot morphology became more
283 compact and had a rounder shape following the dust storm movement.

284 **3.4 Soot-bearing particle size growth following soot aging**

285 The average ratio (D_p/D_{core}) of the diameter of the internally mixed particle (D_p) to
286 its corresponding soot core (D_{core}) during the dust storm period was 1.42 at T1, 1.78 at
287 T2, and 2.49 at T3 (Figure 6b). Size distribution of the soot core indicates a small
288 difference between T1, T2, and T3 during the dust storm period (peak at 200-250 nm,
289 Figure S9). Thus, the D_p/D_{core} increase from T1 to T3 is attributed to the increased
290 coating thickness. The D_p/D_{core} values in this study are much higher than the reported
291 values in fresh emissions (e.g., average value 1.24 for fossil fuel (Sahu et al., 2012))
292 but close to ~ 2.0 in aged aerosols in background and polluted air (Dahlkötter et al.,
293 2014; Raatikainen et al., 2015; Metcalf et al., 2012). Recently, Peng et al. (2017) reported
294 a high growth rate in urban Beijing and a derived average D_p/D_{core} value of 1.97 (1.34-
295 2.61). The D_p/D_{core} value in urban Beijing air is much higher than our reported values
296 of 1.42-1.78 at T1 and T2 during the dust storm period. This is understandable
297 considering the weak secondary aerosol formation in the dust storm in the continental
298 air as a result of acidic gases being scavenged by the large amounts of mineral dust
299 particles (Li et al., 2016b).

300 Based on the air mass backward trajectories, we can infer that it took approximately
301 three hours for the cold front to move between T1 and T2 and 30 hours from T2 to T3
302 (Figure 1). Here, we calculated the coating volume of aged soot particles based on the
303 values of D_p and D_{core} of individual particles and found a 152% increase in the coating
304 volume from T1 to T2 and a 609% increase from T2 to T3.

305 **3.5 Aging mechanism of soot particles**

306 We noticed that the partially embedded soot particles significantly increased from

307 14% at T1 to 68% at T2 (Figure 4), indicating that the fresh soot particles aged during
308 the dust storm movement from the inland to the coastal area. Meanwhile, we found that
309 the D_f value at T1 changed from 1.65 at T1 to 1.84 at T2. The strong diffusion during
310 the dust storm is not conducive to soot accumulation (Pan et al., 2015). Although local
311 emissions at T2 could interference the observation of soot aging process, long-range
312 transported soot particles were still dominant at T2 during the cold front. These results
313 indicate that the morphological structures of soot particles underwent changes along
314 with the dust storm movement. In a word, large amounts of fresh soot converted into
315 partially embedded soot particles from T1 to T2 (Figure 4).

316 Figure 4 shows that the fresh soot particles disappeared at T3, and the number
317 fraction of fully embedded soot particles increased to 84%. Moreover, the D_f of soot
318 particles had a large change from 1.84 at T2 to 1.91 at T3, which suggests that the
319 morphology structure of soot particles changed from chain-like to compact when the
320 air masses crossed the East China Sea (Figure 5).

321 Secondary aerosol formation on soot particles can significantly change their fractal
322 morphology into a compact shape (China et al., 2015; Wang et al., 2017; Ma et al.,
323 2013; Pei et al., 2018). The thick coating of soot particles occurred when air masses
324 crossed the East China Sea (Figure 6b), suggesting that secondary aerosol coating
325 formation can significantly compress the fractal morphology of soot particles. Recently,
326 Yuan et al. (2019) further found that the phase change of secondary aerosols (due to RH
327 variation) in aged soot particles could further compress the fractal shape of soot
328 aggregates. The high humidity in marine air (T2 to T3) should lead to phase changes of
329 secondary aerosols and further cause the morphological compactness of soot
330 aggregations. These two reasons are able to explain the change in soot fractal dimension
331 from T2 to T3 (Figure 5).

332 TEM observations present a particular mixing structure of the fully embedded soot
333 at T3: organic coating instead of sulfate contains several typical soot particles, and the
334 organic coating spreads on the substrate (named droplet-like particles (O'Brien et al.,
335 2015;Li et al., 2011)) (Figures 3d, 7c1-2). More than half of this type of particles contain
336 one or two soot fragments, while 43% of them include more than three soot fragments
337 (Figure S7). The droplet-like coating morphology of soot can reflect that these
338 secondary particles were in an aqueous phase at T3 in the air. Similar droplet-like
339 particles were not observed at T1 and T2 (Figures 7a1-2 and b1-2). A previous study
340 has shown that secondary aerosol particles begin to acquire aqueous shells at RH 60%
341 (Sun et al., 2018). Once secondary aerosols change from a solid to liquid phase
342 following an RH increase in marine air, soot particles tend to adhere to the liquid phase
343 through coagulation (Li et al., 2016b). Figures 7c1-2 show the phase separation of the
344 organic coating and sulfate core on the substrate under the phenomenon of liquid-liquid
345 phase separations (You et al., 2012). Recently, Brunamonti et al. (2015) found that soot
346 particles tend to redistribute into the organic coating during liquid-liquid phase
347 separation. Therefore, the soot distribution in the organic coating indicates that aerosol
348 particles in the air mass at T3 underwent an aqueous aging process over the East China
349 Sea, which is different from the continental aerosol particles at T1 and T2. It must be
350 noted that several tiny soot particles were distributed in the organic coating at T3
351 (Figures 7c1-2), which did not occur at T1 and T2. There is no previous study to report
352 the tiny scattered soot in the organic coating. We proposed a possible reason that soot
353 particle with smaller size have a longer lifetime and could be transported over longer
354 distances. Therefore, the tiny soot particles have more chances to coagulate with
355 preexisting aqueous secondary particles in marine air (Liu et al., 2018). Our findings
356 suggest that the complex aqueous process of individual particles in marine air could

357 result in scattered soot particles, but further studies are required to reveal the detailed
358 reasons.

359 Tracing the soot particles during the dust storm, we can clarify that the morphology
360 change of soot particles depends on the secondary coating thickness and relative
361 humidity in the air. The microscopic changes between soot and coating could change
362 their optical absorption, which is different from the core-shell absorption (He et al.,
363 2015). Our study proposes that BC-related optical models should not only consider the
364 mixing state of soot particles but also incorporate the morphological structure of soot
365 particles in different environmental air.

366 Based on the results and discussion above, we propose a conceptual model to
367 summarize the evolution of morphology and mixing state of soot particles along with
368 the movement of an Asian dust storm (Figure 8). Dust storms in East Asia could carry
369 soot and other anthropogenic pollutants from urban areas to downwind areas. During
370 the transport, the dominated mixing structure of individual soot particles changed from
371 fresh to partially embedded and finally to fully embedded. Meanwhile, the chain-like
372 soot compressed and had a rounder shape depending on secondary coating thickness
373 and relative humidity.

374 **4. Conclusions**

375 Individual aerosol particles were collected from 18 to 19 March 2014 during an
376 Asian dust storm event. Three sampling sites along with the pathway of the dust storm
377 were chosen to study soot aging, including an inland urban site in Jinan city, China (T1),
378 a coastal urban site in Qingdao city, China (T2), and a coastal rural site at Amakusa in
379 southwestern Japan (T3). Soot-bearing particles were classified into three types: fresh,
380 partially embedded, and fully embedded. There was a noticeable difference in the

381 mixing structure of soot particles during long-range transport, with 71% fresh soot in
382 the analyzed soot particles (by number) at T1, 68% partially embedded soot at T2, and
383 84% fully embedded soot at T3. The fractal dimension (D_f) of soot particles at T3 (1.91)
384 was higher than that at the other two sites (1.65 and 1.84), suggesting that soot particles
385 converted from chain-like to compact shapes during long-range transport. This study
386 showed that an increasing number of soot particles were internally mixed with
387 secondary aerosol particles and significantly aged during transport. The average ratio
388 of D_p/D_{core} during the dust storm period was 1.42 at T1, 1.78 at T2, and 2.49 at T3,
389 indicating increasing coating thickness. By comparing the soot fractal dimension in
390 continental air and marine air, we found that secondary coating thickness and relative
391 humidity both can significantly change the fractal morphology of soot particles in the
392 air. Individual particle analysis showed that several tiny soot particles only observed in
393 organic coatings instead of sulfate in individual soot-bearing particles at T3.

394

395 **Data availability**

396 All data presented in this paper are available upon request from the corresponding
397 author (liweijun@zju.edu.cn).

398 **Supporting information**

399 Table S1 and Figures S1-S9

400 **Author contributions**

401 LX and WL conceived the study and wrote the manuscript. The field campaign was
402 organized and supervised by WL and DZ. SF, KM, AN, and TK collected aerosol

403 particles. LX, SS, LL, YW, HN, and ZS contributed sample and data analyses. All
404 authors reviewed and commented on the paper.

405 **Competing interests**

406 The authors declare that they have no conflict of interest.

407 **Acknowledgments**

408 We thank Peter Hyde for his editorial comments. This work was funded by the National Natural
409 Science Foundation of China (42075096, 91844301, 41807305), the National Key R&D Program
410 of China (2017YFC0212700), Zhejiang Provincial Natural Science Foundation of China
411 (LZ19D050001), and China Postdoctoral Science Foundation (2019M662021).

412

413 **References**

- 414 Adachi, K., Moteki, N., Kondo, Y., and Igarashi, Y.: Mixing states of light-absorbing particles measured
415 using a transmission electron microscope and a single-particle soot photometer in Tokyo, Japan, *J.*
416 *Geophys. Res.: Atmos.*, 121, 9153-9164, <https://doi.org/10.1002/2016JD025153>, 2016.
- 417 Bond, T. C., Doherty, S. J., Fahey, D. W., Forster, P. M., Berntsen, T., DeAngelo, B. J., Flanner, M. G.,
418 Ghan, S., Kärcher, B., Koch, D., Kinne, S., Kondo, Y., Quinn, P. K., Sarofim, M. C., Schultz, M. G.,
419 Schulz, M., Venkataraman, C., Zhang, H., Zhang, S., Bellouin, N., Guttikunda, S. K., Hopke, P. K.,
420 Jacobson, M. Z., Kaiser, J. W., Klimont, Z., Lohmann, U., Schwarz, J. P., Shindell, D., Storelvmo, T.,
421 Warren, S. G., and Zender, C. S.: Bounding the role of black carbon in the climate system: A scientific
422 assessment, *J. Geophys. Res.: Atmos.*, 118, 5380-5552, <https://doi.org/10.1002/jgrd.50171>, 2013.
- 423 Brasil, A. M., Farias, T. L., and Carvalho, M. G.: A recipe for image characterization of fractal-Like
424 aggregates, *J. Aerosol Sci*, 30, 1379-1389, [https://doi.org/10.1016/S0021-8502\(99\)00026-9](https://doi.org/10.1016/S0021-8502(99)00026-9), 1999.
- 425 Brunamonti, S., Krieger, U. K., Marcolli, C., and Peter, T.: Redistribution of black carbon in aerosol
426 particles undergoing liquid - liquid phase separation, *Geophys. Res. Lett.*, 42, 2532-2539,
427 <https://doi.org/10.1002/2014GL062908>, 2015.
- 428 Buseck, P. R., Adachi, K., Gelencsér, A., Tompa, É., and Pósfai, M.: Ns-Soot: A Material-Based Term for
429 Strongly Light-Absorbing Carbonaceous Particles, *Aerosol Sci. Technol.*, 48, 777-788,
430 <https://doi.org/10.1080/02786826.2014.919374>, 2014.
- 431 Cappa, C. D., Onasch, T. B., Massoli, P., Worsnop, D. R., Bates, T. S., Cross, E. S., Davidovits, P., Hakala,
432 J., Hayden, K. L., Jobson, B. T., Kolesar, K. R., Lack, D. A., Lerner, B. M., Li, S.-M., Mellon, D.,
433 Nuaaman, I., Olfert, J. S., Petäjä, T., Quinn, P. K., Song, C., Subramanian, R., Williams, E. J., and
434 Zaveri, R. A.: Radiative Absorption Enhancements Due to the Mixing State of Atmospheric Black
435 Carbon, *Science*, 337, 1078-1081, <https://doi.org/10.1126/science.1223447>, 2012.
- 436 Chakrabarty, R. K., Moosmüller, H., Garro, M. A., Arnott, W. P., Walker, J., Susott, R. A., Babbitt, R. E.,
437 Wold, C. E., Lincoln, E. N., and Hao, W. M.: Emissions from the laboratory combustion of wildland

438 fuels: Particle morphology and size, *J. Geophys. Res.: Atmos.*, 111,
439 <https://doi.org/10.1029/2005JD006659>, 2006.

440 Chi, J. W., Li, W. J., Zhang, D. Z., Zhang, J. C., Lin, Y. T., Shen, X. J., Sun, J. Y., Chen, J. M., Zhang, X.
441 Y., Zhang, Y. M., and Wang, W. X.: Sea salt aerosols as a reactive surface for inorganic and organic
442 acidic gases in the Arctic troposphere, *Atmos. Chem. Phys.*, 15, 11341-11353,
443 <https://doi.org/10.5194/acp-15-11341-2015>, 2015.

444 China, S., Mazzoleni, C., Gorkowski, K., Aiken, A. C., and Dubey, M. K.: Morphology and mixing state
445 of individual freshly emitted wildfire carbonaceous particles, *Nat. Commun.*, 4, 2122,
446 <https://doi.org/10.1038/ncomms3122>, 2013.

447 China, S., Scarnato, B., Owen, R. C., Zhang, B., Ampadu, M. T., Kumar, S., Dzepina, K., Dziobak, M.
448 P., Fialho, P., and Perlinger, J. A.: Morphology and mixing state of aged soot particles at a remote
449 marine free troposphere site: Implications for optical properties, *Geophys. Res. Lett.*, 42, 1243-1250,
450 <https://doi.org/10.1002/2014GL062404>, 2015.

451 Dahlkötter, F., Gysel, M., Sauer, D., Minikin, A., Baumann, R., Seifert, P., Ansmann, A., Fromm, M.,
452 Voigt, C., and Weinzierl, B.: The Pagami Creek smoke plume after long-range transport to the upper
453 troposphere over Europe – aerosol properties and black carbon mixing state, *Atmos. Chem.*
454 *Phys.*, 14, 6111-6137, <https://doi.org/10.5194/acp-14-6111-2014>, 2014.

455 Ding, A. J., Huang, X., Nie, W., Sun, J. N., Kerminen, V. M., Petäjä, T., Su, H., Cheng, Y. F., Yang, X.
456 Q., Wang, M. H., Chi, X. G., Wang, J. P., Virkkula, A., Guo, W. D., Yuan, J., Wang, S. Y., Zhang, R.
457 J., Wu, Y. F., Song, Y., Zhu, T., Zilitinkevich, S., Kulmala, M., and Fu, C. B.: Enhanced haze pollution
458 by black carbon in megacities in China, *Geophys. Res. Lett.*, 43, 2873-2879,
459 <https://doi.org/10.1002/2016GL067745>, 2016.

460 Ding, S., Liu, D., Zhao, D., Hu, K., Tian, P., Zhou, W., Huang, M., Yang, Y., Wang, F., Sheng, J., Liu, Q.,
461 Kong, S., Cui, P., Huang, Y., He, H., Coe, H., and Ding, D.: Size-Related Physical Properties of Black
462 Carbon in the Lower Atmosphere over Beijing and Europe, *Environ. Sci. Technol.*, 53, 11112-11121,
463 <https://doi.org/10.1021/acs.est.9b03722>, 2019.

464 Geng, H., Hwang, H., Liu, X., Dong, S., and Ro, C. U.: Investigation of aged aerosols in size-resolved
465 Asian dust storm particles transported from Beijing, China, to Incheon, Korea, using low-Z particle
466 EPMA, *Atmos. Chem. Phys.*, 14, 3307-3323, <https://doi.org/10.5194/acp-14-3307-2014>, 2014.

467 He, C., Liou, K. N., Takano, Y., Zhang, R., Levy Zamora, M., Yang, P., Li, Q., and Leung, L. R.: Variation
468 of the radiative properties during black carbon aging: theoretical and experimental intercomparison,
469 *Atmos. Chem. Phys.*, 15, 11967-11980, <https://doi.org/10.5194/acp-15-11967-2015>, 2015.

470 Healy, R. M., Riemer, N., Wenger, J. C., Murphy, M., West, M., Poulain, L., Wiedensohler, A., O'Connor,
471 I. P., McGillicuddy, E., Sodeau, J. R., and Evans, G. J.: Single particle diversity and mixing state
472 measurements, *Atmos. Chem. Phys.*, 14, 6289-6299, <https://doi.org/10.5194/acp-14-6289-2014>, 2014.

473 IPCC.: Clouds and Aerosols. In: *Climate Change 2013: The Physical Science Basis, Contribution of*
474 *Working Group I to the Fifth Assessment Report of the Intergovernmental Panel on Climate Change.*
475 *Intergovernmental Panel on Climate Change (IPCC)*, 571- 657, 2013.

476 Jacobson, M. Z.: Strong radiative heating due to the mixing state of black carbon in atmospheric aerosols,
477 *Nature*, 409, 695-697, <https://doi.org/10.1038/35055518>, 2001.

478 Koeylue, U., Xing, Y., and Rosner, D. E.: Fractal Morphology Analysis of Combustion-Generated
479 Aggregates Using Angular Light Scattering and Electron Microscope Images, *Langmuir*, 11, 4848-
480 4854, <https://doi.org/10.1021/la00012a043>, 1995.

481 Laskin, A., Moffet, R. C., and Gilles, M. K.: Chemical Imaging of Atmospheric Particles, *Acc. Chem.*

482 Res., 52, 3419-3431, <https://doi.org/10.1021/acs.accounts.9b00396>, 2019.

483 Lee, A. K. Y., Rivellini, L.-H., Chen, C.-L., Liu, J., Price, D. J., Betha, R., Russell, L. M., Zhang, X., and
484 Cappa, C. D.: Influences of Primary Emission and Secondary Coating Formation on the Particle
485 Diversity and Mixing State of Black Carbon Particles, *Environ. Sci. Technol.*, 53, 9429-9438,
486 <https://doi.org/10.1021/acs.est.9b03064>, 2019.

487 Li, J., Liu, C., Yin, Y., and Kumar, K. R.: Numerical investigation on the Ångström exponent of black
488 carbon aerosol, *J. Geophys. Res.: Atmos.*, 121, 3506-3518, <https://doi.org/10.1002/2015JD024718>,
489 2016a.

490 Li, W., Zhou, S., Wang, X., Xu, Z., Yuan, C., Yu, Y., Zhang, Q., and Wang, W.: Integrated evaluation of
491 aerosols from regional brown hazes over northern China in winter: Concentrations, sources,
492 transformation, and mixing states, *J. Geophys. Res.: Atmos.*, 116, D09301,
493 <https://doi.org/10.1029/2010JD015099>, 2011.

494 Li, W., Shao, L., Shi, Z., Chen, J., Yang, L., Yuan, Q., Yan, C., Zhang, X., Wang, Y., Sun, J., Zhang, Y.,
495 Shen, X., Wang, Z., and Wang, W.: Mixing state and hygroscopicity of dust and haze particles before
496 leaving Asian continent, *J. Geophys. Res.: Atmos.*, 119, 1044-1059,
497 <https://doi.org/10.1002/2013JD021003>, 2014.

498 Li, W., Sun, J., Xu, L., Shi, Z., Riemer, N., Sun, Y., Fu, P., Zhang, J., Lin, Y., Wang, X., Shao, L., Chen,
499 J., Zhang, X., Wang, Z., and Wang, W.: A conceptual framework for mixing structures in individual
500 aerosol particles, *J. Geophys. Res.: Atmos.*, 121, 13784-13798,
501 <https://doi.org/10.1002/2016JD025252>, 2016b.

502 Liu, D., Whitehead, J., Alfarra, M. R., Reyes-Villegas, E., Spracklen, D. V., Reddington, C. L., Kong, S.,
503 Williams, P. I., Ting, Y.-C., Haslett, S., Taylor, J. W., Flynn, M. J., Morgan, W. T., McFiggans, G.,
504 Coe, H., and Allan, J. D.: Black-carbon absorption enhancement in the atmosphere determined by
505 particle mixing state, *Nat. Geosci.*, 10, 184-188, <https://doi.org/10.1038/ngeo2901>, 2017.

506 Liu, L., Zhang, J., Xu, L., Yuan, Q., Huang, D., Chen, J., Shi, Z., Sun, Y., Fu, P., Wang, Z., Zhang, D.,
507 and Li, W.: Cloud scavenging of anthropogenic refractory particles at a mountain site in North China,
508 *Atmos. Chem. Phys.*, 18, 14681-14693, <https://doi.org/10.5194/acp-18-14681-2018>, 2018.

509 Ma, X., Zangmeister, C. D., Gigault, J., Mulholland, G. W., and Zachariah, M. R.: Soot aggregate
510 restructuring during water processing, *J. Aerosol Sci.*, 66, 209-219,
511 <https://doi.org/10.1016/j.jaerosci.2013.08.001>, 2013.

512 Matsui, H., Hamilton, D. S., and Mahowald, N. M.: Black carbon radiative effects highly sensitive to
513 emitted particle size when resolving mixing-state diversity, *Nat. Commun.*, 9, 3446,
514 <https://doi.org/10.1038/s41467-018-05635-1>, 2018.

515 Metcalf, A. R., Craven, J. S., Ensberg, J. J., Brioude, J., Angevine, W., Sorooshian, A., Duong, H. T.,
516 Jonsson, H. H., Flagan, R. C., and Seinfeld, J. H.: Black carbon aerosol over the Los Angeles Basin
517 during CalNex, *J. Geophys. Res.: Atmos.*, 117, D00V13, <https://doi.org/10.1029/2011JD017255>,
518 2012.

519 Moffet, R. C., and Prather, K. A.: In-situ measurements of the mixing state and optical properties of soot
520 with implications for radiative forcing estimates, *Proc. Natl. Acad. Sci. U.S.A.*, 106, 11872-11877,
521 <https://doi.org/10.1073/pnas.0900040106>, 2009.

522 O'Brien, R. E., Wang, B., Kelly, S. T., Lundt, N., You, Y., Bertram, A. K., Leone, S. R., Laskin, A., and
523 Gilles, M. K.: Liquid-Liquid Phase Separation in Aerosol Particles: Imaging at the Nanometer Scale,
524 *Environ. Sci. Technol.*, 49, 4995-5002, <https://doi.org/10.1021/acs.est.5b00062>, 2015.

525 Oh, C., and Sorensen, C. M.: The Effect of Overlap between Monomers on the Determination of Fractal

526 Cluster Morphology, *J. Colloid Interface Sci.*, 193, 17-25, <https://doi.org/10.1006/jcis.1997.5046>,
527 1997.

528 Pan, X., Uno, I., Hara, Y., Kuribayashi, M., Kobayashi, H., Sugimoto, N., Yamamoto, S., Shimohara, T.,
529 and Wang, Z.: Observation of the simultaneous transport of Asian mineral dust aerosols with
530 anthropogenic pollutants using a POPC during a long-lasting dust event in late spring 2014, *Geophys.*
531 *Res. Lett.*, 42, 1593-1598, <https://doi.org/10.1002/2014GL062491>, 2015.

532 Pei, X., Hallquist, M., Eriksson, A. C., Pagels, J., Donahue, N. M., Mentel, T., Svenningsson, B., Brune,
533 W., and Pathak, R. K.: Morphological transformation of soot: investigation of microphysical
534 processes during the condensation of sulfuric acid and limonene ozonolysis product vapors, *Atmos.*
535 *Chem. Phys.*, 18, 9845-9860, <https://doi.org/10.5194/acp-18-9845-2018>, 2018.

536 Peng, J., Hu, M., Guo, S., Du, Z., Shang, D., Zheng, J., Zheng, J., Zeng, L., Shao, M., Wu, Y., Collins,
537 D., and Zhang, R.: Ageing and hygroscopicity variation of black carbon particles in Beijing measured
538 by a quasi-atmospheric aerosol evolution study (QUALITY) chamber, *Atmos. Chem. Phys.*, 17,
539 10333-10348, <https://doi.org/10.5194/acp-17-10333-2017>, 2017.

540 Perring, A. E., Schwarz, J. P., Markovic, M. Z., Fahey, D. W., Jimenez, J. L., Campuzano-Jost, P., Palm,
541 B. D., Wisthaler, A., Mikoviny, T., Diskin, G., Sachse, G., Ziemba, L., Anderson, B., Shingler, T.,
542 Crosbie, E., Sorooshian, A., Yokelson, R., and Gao, R.-S.: In situ measurements of water uptake by
543 black carbon-containing aerosol in wildfire plumes, *J. Geophys. Res.: Atmos.*, 122, 1086-1097,
544 <https://doi.org/10.1002/2016JD025688>, 2017.

545 Raatikainen, T., Brus, D., Hyvärinen, A. P., Svensson, J., Asmi, E., and Lihavainen, H.: Black carbon
546 concentrations and mixing state in the Finnish Arctic, *Atmos. Chem. Phys.*, 15, 10057-10070,
547 <https://doi.org/10.5194/acp-15-10057-2015>, 2015.

548 Riemer, N., West, M., Zaveri, R., and Easter, R.: Estimating black carbon aging time-scales with a
549 particle-resolved aerosol model, *J. Aerosol Sci.*, 41, 143-158,
550 <https://doi.org/10.1016/j.jaerosci.2009.08.009>, 2010.

551 Riemer, N., and West, M.: Quantifying aerosol mixing state with entropy and diversity measures, *Atmos.*
552 *Chem. Phys.*, 13, 11423-11439, <https://doi.org/10.5194/acp-13-11423-2013>, 2013.

553 Sahu, L. K., Kondo, Y., Moteki, N., Takegawa, N., Zhao, Y., Cubison, M. J., Jimenez, J. L., Vay, S.,
554 Diskin, G. S., Wisthaler, A., Mikoviny, T., Huey, L. G., Weinheimer, A. J., and Knapp, D. J.: Emission
555 characteristics of black carbon in anthropogenic and biomass burning plumes over California during
556 ARCTAS-CARB 2008, *J. Geophys. Res.: Atmos.*, 117, D16302,
557 <https://doi.org/10.1029/2011JD017401>, 2012.

558 Shiraiwa, M., Kondo, Y., Moteki, N., Takegawa, N., Miyazaki, Y., and Blake, D. R.: Evolution of mixing
559 state of black carbon in polluted air from Tokyo, *Geophys. Res. Lett.*, 34, L16803,
560 <https://doi.org/10.1029/2007GL029819>, 2007.

561 Stein, A. F., Draxler, R. R., Rolph, G. D., Stunder, B. J. B., Cohen, M. D., and Ngan, F.: NOAA's
562 HYSPLIT Atmospheric Transport and Dispersion Modeling System, *Bull. Amer. Meteor. Soc.*, 96,
563 2059-2077, <https://doi.org/10.1175/bams-d-14-00110.1>, 2015.

564 Sun, J., Liu, L., Xu, L., Wang, Y., Wu, Z., Hu, M., Shi, Z., Li, Y., Zhang, X., Chen, J., and Li, W.: Key
565 Role of Nitrate in Phase Transitions of Urban Particles: Implications of Important Reactive Surfaces
566 for Secondary Aerosol Formation, *J. Geophys. Res.: Atmos.*, 123, 1234-1243,
567 <https://doi.org/10.1002/2017JD027264>, 2018.

568 Ueda, S., Nakayama, T., Taketani, F., Adachi, K., Matsuki, A., Iwamoto, Y., Sadanaga, Y., and Matsumi,
569 Y.: Light absorption and morphological properties of soot-containing aerosols observed at an East

570 Asian outflow site, Noto Peninsula, Japan, *Atmos. Chem. Phys.*, 16, 2525-2541,
571 <https://doi.org/10.5194/acp-16-2525-2016>, 2016.

572 Wang, J., Cubison, M. J., Aiken, A. C., Jimenez, J. L., and Collins, D. R.: The importance of aerosol
573 mixing state and size-resolved composition on CCN concentration and the variation of the importance
574 with atmospheric aging of aerosols, *Atmos. Chem. Phys.*, 10, 7267-7283, <https://doi.org/10.5194/acp-10-7267-2010>, 2010.

576 Wang, Y., Liu, F., He, C., Bi, L., Cheng, T., Wang, Z., Zhang, H., Zhang, X., Shi, Z., and Li, W.: Fractal
577 Dimensions and Mixing Structures of Soot Particles during Atmospheric Processing, *Environ. Sci.
578 Technol. Lett.*, 4, 487-493, <https://doi.org/10.1021/acs.estlett.7b00418>, 2017.

579 Wentzel, M., Gorzawski, H., Naumann, K. H., Saathoff, H., and Weinbruch, S.: Transmission electron
580 microscopical and aerosol dynamical characterization of soot aerosols, *J. Aerosol Sci.*, 34, 1347-1370,
581 [https://doi.org/10.1016/S0021-8502\(03\)00360-4](https://doi.org/10.1016/S0021-8502(03)00360-4), 2003.

582 West, J. J., Cohen, A., Dentener, F., Brunekreef, B., Zhu, T., Armstrong, B., Bell, M. L., Brauer, M.,
583 Carmichael, G., Costa, D. L., Dockery, D. W., Kleeman, M., Krzyzanowski, M., Künzli, N., Liousse,
584 C., Lung, S.-C. C., Martin, R. V., Pöschl, U., Pope, C. A., Roberts, J. M., Russell, A. G., and
585 Wiedinmyer, C.: “What We Breathe Impacts Our Health: Improving Understanding of the Link
586 between Air Pollution and Health”, *Environ. Sci. Technol.*, 50, 4895-4904,
587 <https://doi.org/10.1021/acs.est.5b03827>, 2016.

588 Wu, Y., Cheng, T., Liu, D., Allan, J. D., Zheng, L., and Chen, H.: Light Absorption Enhancement of Black
589 Carbon Aerosol Constrained by Particle Morphology, *Environ. Sci. Technol.*, 52, 6912-6919,
590 <https://doi.org/10.1021/acs.est.8b00636>, 2018.

591 Xu, L., Zhang, D., and Li, W.: Microscopic comparison of aerosol particles collected at an urban site in
592 North China and a coastal site in Japan, *Sci. Total Environ.*, 669, 948-954,
593 <https://doi.org/10.1016/j.scitotenv.2019.03.163>, 2019.

594 You, Y., Renbaum-Wolff, L., Carreras-Sospedra, M., Hanna, S. J., Hiranuma, N., Kamal, S., Smith, M.
595 L., Zhang, X., Weber, R. J., Shilling, J. E., Dabdub, D., Martin, S. T., and Bertram, A. K.: Images
596 reveal that atmospheric particles can undergo liquid-liquid phase separations, *Proc. Natl. Acad. Sci.
597 U.S.A.*, 109, 13188-13193, <https://doi.org/10.1073/pnas.1206414109>, 2012.

598 Yuan, Q., Xu, J., Wang, Y., Zhang, X., Pang, Y., Liu, L., Bi, L., Kang, S., and Li, W.: Mixing State and
599 Fractal Dimension of Soot Particles at a Remote Site in the Southeastern Tibetan Plateau, *Environ.
600 Sci. Technol.*, 53, 8227-8234, <https://doi.org/10.1021/acs.est.9b01917>, 2019.

601 Zhang, D., Iwasaka, Y., Shi, G., Zang, J., Hu, M., and Li, C.: Separated status of the natural dust plume
602 and polluted air masses in an Asian dust storm event at coastal areas of China, *J. Geophys. Res.:
603 Atmos.*, 110, D06302, <https://doi.org/10.1029/2004JD005305>, 2005.

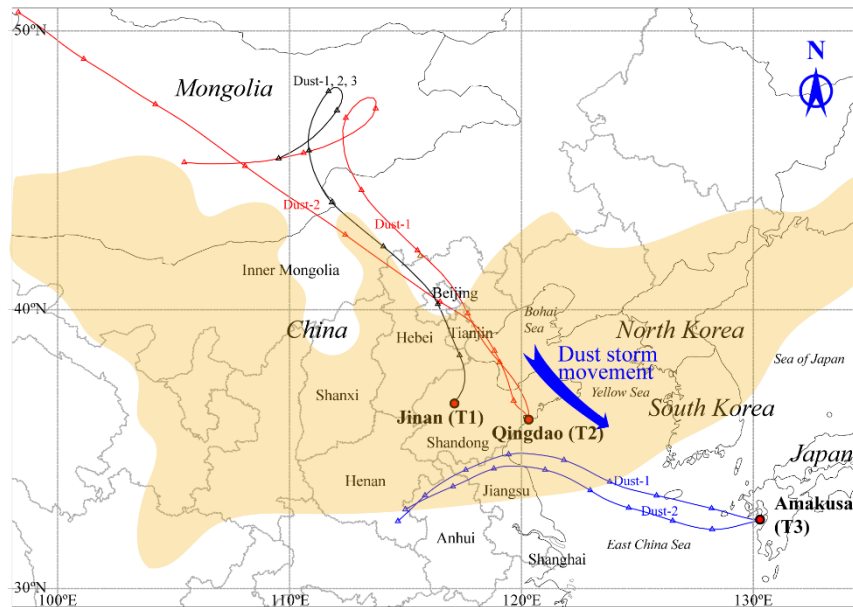
604 Zhang, G., Bi, X., Li, L., Chan, L. Y., Li, M., Wang, X., Sheng, G., Fu, J., and Zhou, Z.: Mixing state of
605 individual submicron carbon-containing particles during spring and fall seasons in urban Guangzhou,
606 China: a case study, *Atmos. Chem. Phys.*, 13, 4723-4735, <https://doi.org/10.5194/acp-13-4723-2013>,
607 2013.

608 Zhang, R., Khalizov, A. F., Pagels, J., Zhang, D., Xue, H., and McMurry, P. H.: Variability in morphology,
609 hygroscopicity, and optical properties of soot aerosols during atmospheric processing, *Proc. Natl.
610 Acad. Sci. U.S.A.*, 105, 10291-10296, <https://doi.org/10.1073/pnas.0804860105>, 2008.

611 Zhang, X., Mao, M., Yin, Y., and Wang, B.: Numerical Investigation on Absorption Enhancement of
612 Black Carbon Aerosols Partially Coated With Nonabsorbing Organics, *J. Geophys. Res.: Atmos.*, 123,
613 1297-1308, <https://doi.org/10.1002/2017JD027833>, 2018a.

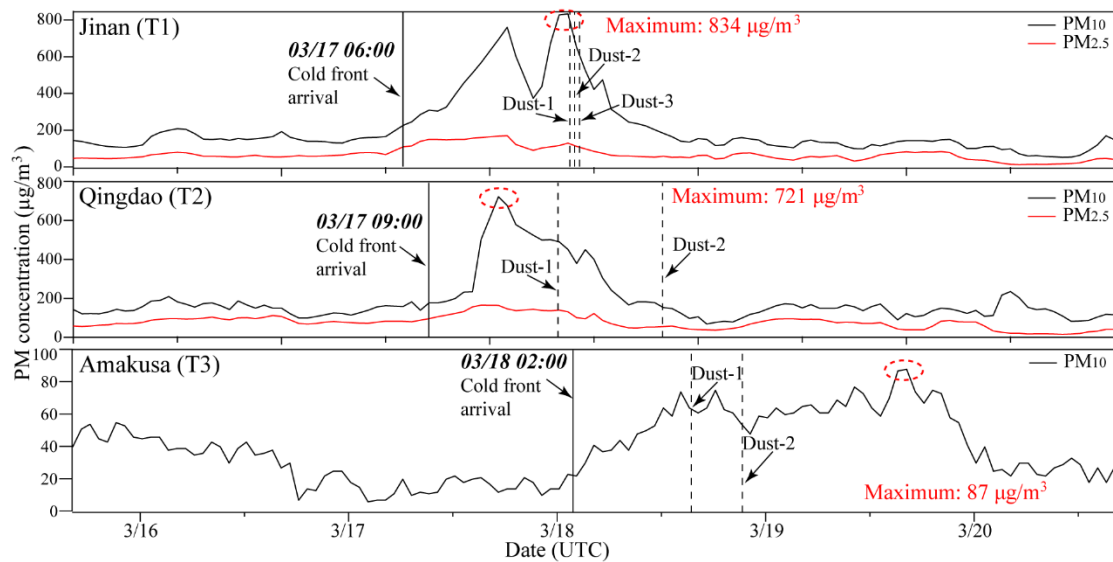
614 Zhang, Y., Su, H., Ma, N., Li, G., Kecorius, S., Wang, Z., Hu, M., Zhu, T., He, K., Wiedensohler, A.,
615 Zhang, Q., and Cheng, Y.: Sizing of Ambient Particles From a Single-Particle Soot Photometer
616 Measurement to Retrieve Mixing State of Black Carbon at a Regional Site of the North China Plain,
617 *J. Geophys. Res.: Atmos.*, 123, 778-795, <https://doi.org/10.1029/2018JD028810>, 2018b.

618



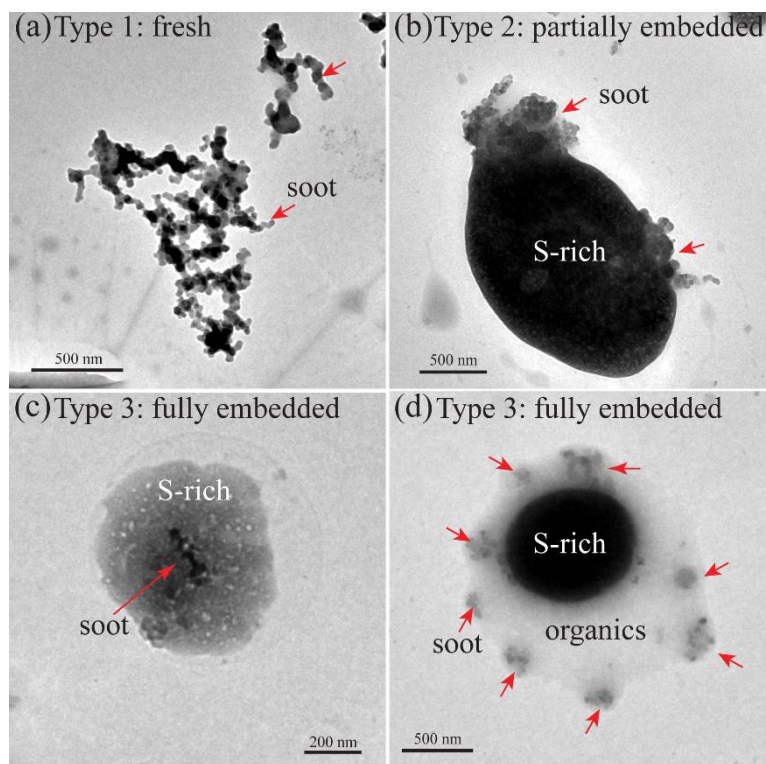
619

620 Figure 1. The locations of the three sampling sites and HYSPLIT forty-eight hour air
 621 mass backward trajectories arriving at 1500 m above ground level at T1, T2, and T3
 622 sites. The interval between two triangle symbols is six hours. The yellow shadow is
 623 derived from Figure S1, which represents the area influenced by the dust storm at 00:00
 624 on 2014/03/18 (UTC).



625

626 Figure 2. Time series of PM (particulate matter) concentrations at T1, T2, and T3 during
 627 sampling. The cold front arrival times indicate the time when the sampling site starts to
 628 be influenced by the dust storm. Data sources: T1 and T2: The Ministry of Ecology and
 629 Environment of the People's Republic of China, <https://www.aqistudy.cn/>; T3: National
 630 Institute for Environmental Studies of Japan, <https://www.nies.go.jp/igreen/>.

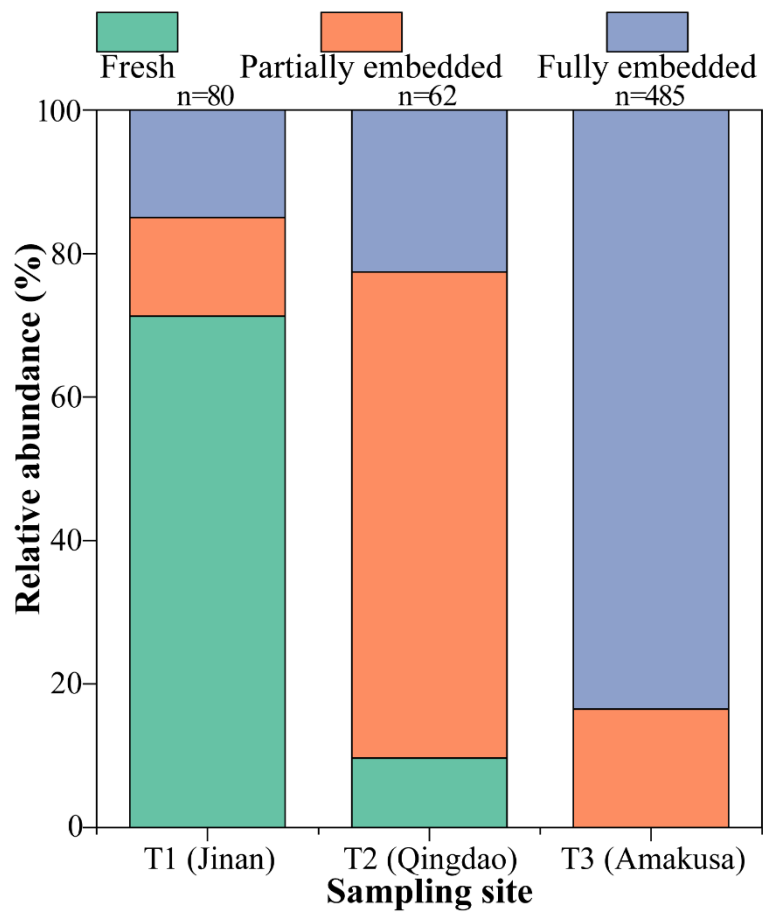


631

632 Figure 3. Morphology of soot-bearing aerosol particles: (a) fresh chain-like soot
 633 aggregates with no visible coating; (b) partially embedded soot: part of the soot particle
 634 was coated by secondary aerosols; (c) fully embedded soot: the whole soot particle was
 635 encapsulated by secondary aerosols; (d) a subtype of fully embedded soot: individual
 636 soot particles were only embedded in the organic coating on a sulfur-rich particle.

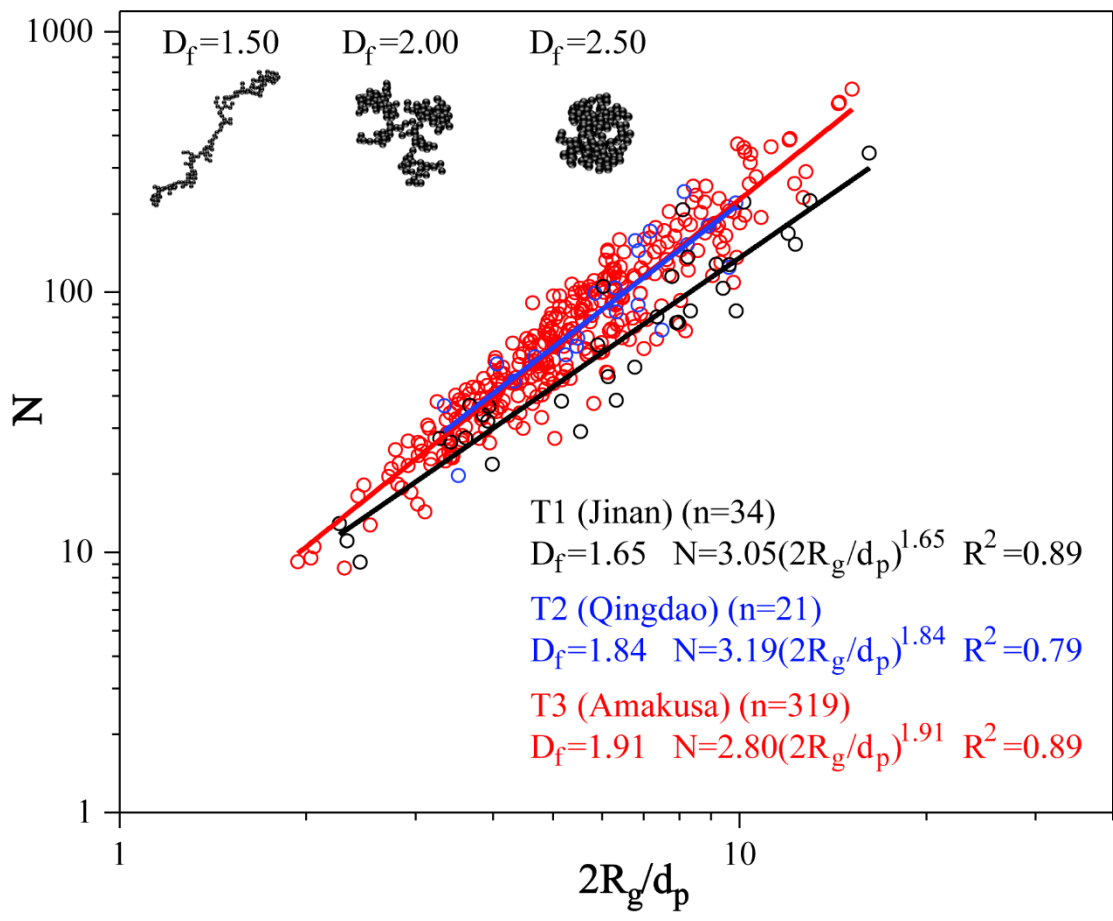
637

638



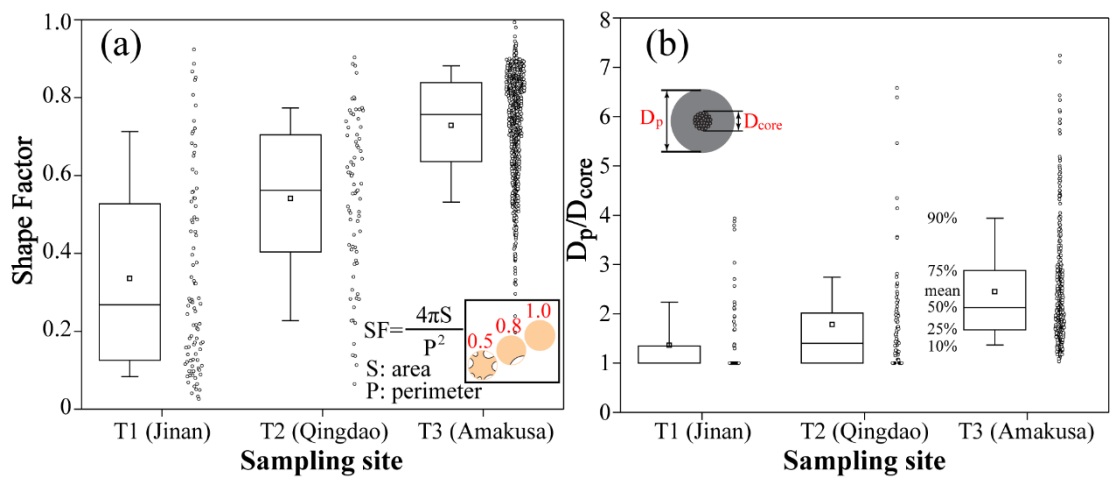
639

640 Figure 4. Relative abundance of three types of soot-bearing aerosol particles at the three
 641 sampling sites. The number of analyzed soot-bearing particles is shown above the
 642 column.



643
644
645
646
647
648
649
650
651

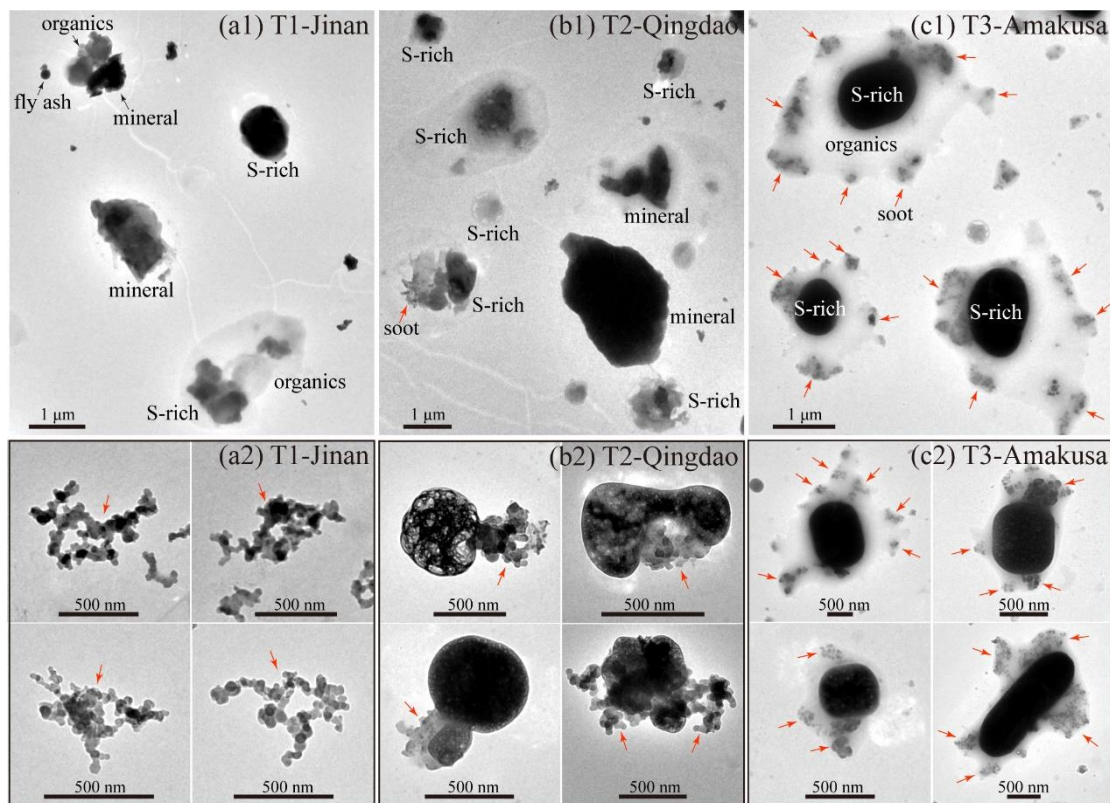
Figure 5. Fractal dimension of soot-bearing particles at the three sampling sites. The parameter n in parentheses represents the total number of soot particles analyzed for each site to calculate D_f and k_g . Three model simulated soot particles with different D_f are presented to represent different soot morphology. The inconsistency of analyzed soot number in Figure 4 and 5 is attributed to the indistinct soot particles in the low-magnification TEM images that can be identified as soot but cannot provide necessary data for D_f analysis.



652

653 Figure 6. (a) Shape factor of soot-bearing particles and (b) the particle-to-soot core
 654 diameter ratio (D_p/D_{core}) at the three sampling sites.

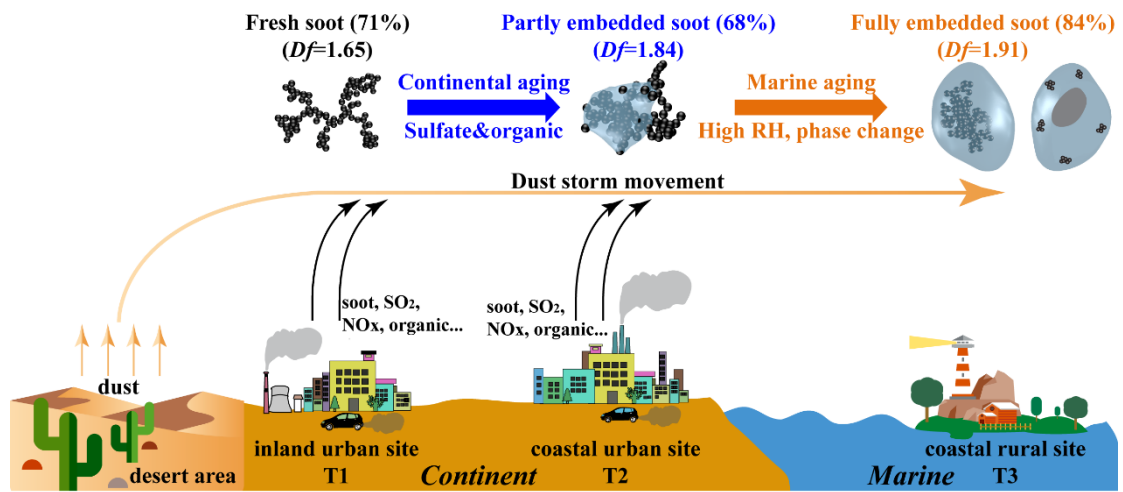
655



656

657 Figure 7. (a1-c1) Low-magnification TEM images at T1, T2, and T3. (a2-c2) TEM
 658 images of dominated soot type at T1, T2, and T3.

659



660

661 Figure 8. Schematic diagram showing the evolution of morphology and mixing state of

662 soot particles along with the movement of an Asian dust storm.